Mechanics of microtubule organizing center clustering and spindle positioning in budding yeast *Cryptococcus neoformans*

Saptarshi Chatterjee,[1,*] Subhendu Som,[1,†] Neha Varshney,[2,‡] PVS Satyadev,[2,§] Kaustuv Sanyal,[2,‖] and Raja Paul[1,¶]

[1]*Indian Association for the Cultivation of Science, Kolkata-700032, India*

[2]*Molecular Mycology Laboratory, Molecular Biology and Genetics Unit, Jawaharlal Nehru Centre for Advanced Scientific Research, Jakkur, Bangalore 560064, India*

(Received 31 March 2021; accepted 9 August 2021; published 3 September 2021)

The dynamic process of mitotic spindle assembly depends on multitudes of inter-dependent interactions involving kinetochores (KTs), microtubules (MTs), spindle pole bodies (SPBs), and molecular motors. Before forming the mitotic spindle, multiple visible microtubule organizing centers (MTOCs) coalesce into a single focus to serve as an SPB in the pathogenic budding yeast, *Cryptococcus neoformans*. To explain this unusual phenomenon in the fungal kingdom, we propose a "search and capture" model, in which cytoplasmic MTs (cMTs) nucleated by MTOCs grow and capture each other to promote MTOC clustering. Our quantitative modeling identifies multiple redundant mechanisms mediated by a combination of cMT-cell cortex interactions and inter-cMT coupling to facilitate MTOC clustering within the physiological time limit as determined by time-lapse live-cell microscopy. Besides, we screen various possible mechanisms by computational modeling and propose optimal conditions that favor proper spindle positioning—a critical determinant for timely chromosome segregation. These analyses also reveal that a combined effect of MT buckling, dynein pull, and cortical push maintains spatiotemporal spindle localization.

DOI: 10.1103/PhysRevE.104.034402

I. INTRODUCTION

Spatiotemporal dynamics of organelle-constituents relies primarily on the active organization of microtubules (MTs). MTs are semiflexible polymeric filaments having rapidly polymerizing plus ends and slowly polymerizing minus ends. The growth and shrinkage of MTs are governed by intrinsic dynamic instability parameters [1]. In animal cells, the centrosome is a major MT nucleating center which forms a radial MT array [2–4] along with other membrane organelles such as the Golgi apparatus facilitating many noncentrosomal, radial MT networks [2,5–9]. The cellular structures that harbor the ability to nucleate MTs and organize a radial network are often referred to as microtubule organizing centers (MTOCs) [2,10].

In the ascomycete budding yeast *Saccharomyces cerevisiae*, spindle pole bodies (SPBs), embedded on the nuclear envelope (NE) are analogous to centrosomes. The SPBs nucleate and organize the cytoplasmic MTs (cMTs) and nuclear MTs (nMTs) [11,12]. Similarly, a single MTOC in basidiomycete budding yeast *Cryptococcus neoformans* can accommodate nucleation sites for both cMTs and nMTs [2,10,13]. Note that the meaning and the context of various biological terms are elucidated in Table I.

There exists two major fungal phyla, Ascomycota and Basidiomycota [14–16] that shared a common ancestor more than 500 million years ago [17]. While extensive studies have been carried out in the context of cell division in ascomycetous budding yeasts such as *S. cerevisiae*, the process of chromosomal partitioning in organisms belonging to Basidiomycota remains under-studied [14–16,18]. A relatively better model basidiomycetous budding yeast is *C. neoformans*, a human pathogen. Like *S. cerevisiae*, cells divide by budding in *C. neoformans* as well (Fig. 1(a), Movie M1 in the Supplemental Material [19]). The major sequence of mitotic events from the formation of bud until chromosome segregation in *C. neoformans* can be categorized in the following temporal order: (a) Bud inception at the end of G1/onset of S phase [16], (b) clustering of KTs as a single punctum at the periphery of the nucleus after bud initiation [16] (Fig. 1(a), Movie M1 in the Supplemental Material [19]), (c) nuclear migration into the daughter bud followed by spindle formation, (d) localization of the spindle near the bud-neck junction/septin ring [Fig. 1(a)], and eventually (e) equal nuclear division mother and daughter bud (Fig. 1(a), Movie M1 in the Supplemental Material [19]). Note that, in contrast to *S. cerevisiae*, where the SPB being the only MTOC, several MTOCs are present in the basidiomycete budding yeast *C. neoformans* during interphase [14,20,21] [Fig. 1(b)]. Moreover, in *C. neoformans*, KTs are unclustered during interphase [15,16,20]. As the cell advances through the cell cycle, the KTs gradually cluster into a single punctum, plausibly via various MT-mediated interactions. Interestingly, a previous study [20] as well as our experiments [Figs. 1(b)–1(d)] identify that the KTs colocalize with the MTOCs. The clustering

*sspsc6@iacs.res.in
†subhendu.som@gmail.com
‡neha.var15@gmail.com
§pvssdev@jncasr.ac.in
‖sanyal@jncasr.ac.in
¶Corresponding author: raja.paul@iacs.res.in

TABLE I. *Dictionary* of biological terms to summarize their relevance in this study.

Biological term	Meaning	Role in the modeling template
Dynein	-ve end directed molecular motor	When MTs slide inside the cell cortex, dyneins impart a directed pull on the MTs.
Bim1	MT associated protein (MAP), protein that bind to MT	In coarse-grained simulations, Bim1 effectively engineers a force bias on the MT segments inside mother cell cortex toward the septin ring.
Microtubule (MT)	A type of polar filament constituting cell cytoskeleton. MTs are one of the major building blocks of the mitotic spindle.	All force interactions in the models are orchestrated on and/or transduced via MTs.
MTOC	Microtubule Organizing Center; MTs nucleate and grow from MTOCs.	In *C. neoformans*, there are multiple MTOCs at bud initiation. MTOCs cluster to form SPB. In simulations, they are MT nucleating spherical objects constrained to move on NE.
SPB	Spindle Pole Body; MTs nucleate and grow from SPBs.	In simulations, they are MT nucleating spherical objects constrained to move on NE.
Spindle	Molecular machine that facilitates cell division	In simulations, the spindle is a dynamic emergent structure comprising mainly SPBs, MTs and chromosomes.
Septin ring	The protein complex septin forms a ring shaped assembly on plasma membrane at bud neck junction.	In simulations, it is the circular intersection/junction between mother and daughter bud which are modeled as intersecting spheres.
Minus end directed motor	molecular motors that walk toward MT minus end	In antiparallel MT-MT overlap, crosslinking minus end directed motors generate a net attraction between MT minus ends. In simulations, since MT minus ends are anchored at MTOCs, two MTOCs at an antiparallel overlap approach each other due to this motor interaction.

of KTs into a single punctum and the clustering of MTOCs into a single SPB happen concomitantly [Figs. 1(b)–1(d)]. In *S. cerevisiae*, before the chromosome segregation, the nucleus migrates to the proximity of the mother-daughter bud neck junction [14,16,22]. In *C. neoformans*, the sequence of events characterizing nuclear migration before the division is somewhat different from those of *S. cerevisiae*. First, the nucleus entirely moves to the daughter bud (Fig. S1 in the Supplemental Material [19]). Second, the SPB duplication occurs either in the daughter bud or when the nucleus is migrated close to the bud-neck junction (namely the septin ring), as depicted in Figs. 1(b) and 1(d). Subsequently, SPB biorientation, spindle formation, and localization of the spindle structure *inside the daughter bud near the septin ring* pave the way for proper division [14–16]. While framing a mechanistic model of mitotic division in budding yeast *C. neoformans*, we took a cue from our previous studies [14,16] and extended the ideas of various force interactions from another budding yeast *S. cerevisiae* for its geometric similarity and similarities in cell cycle stages that lead to chromosome segregation.

Self-assembly of MTOCs is orchestrated by MT mediated "search and capture" mechanism [14,16]. Essential characteristics of the clustering mechanisms are shared across a diverse set of organisms as well as several organelle assemblies (e.g., Golgi assembly and stacking, mitochondrial assembly, multi-centrosomal clustering [23], etc.) and are not necessarily organism-specific [8]. The mechanics of MTOC clustering before the formation of the SPB in *C. neoformans* remains elusive and deciphering the same experimentally is challenging. The complete clustering in wild-type cells occurs within ∼25 min since bud initiation [Figs. 1(e) and 1(f)]. In this context, we attempted to simulate possible mechanisms of MTOC clustering within the physiological time limit as determined experimentally by time-lapse microscopy.

In budding yeast *S. cerevisiae*, location for the mitotic division is predetermined even before forming the spindle [14,24]. In *C. neoformans*, the spindle is formed and stabilizes near the septin ring within the daughter bud [16] (Fig. 1(a), Fig. S1 in the Supplemental Material [19], Movie M1 in the Supplemental Material [19]). The event is preceded by the migration of the nucleus [16,25] as determined from the statistics in Fig. S1 in the Supplemental Material [19]. Timely nuclear migration into the daughter bud requires directed force generation toward the daughter bud. Since the proper positioning of the spindle and its alignment are crucial determinants of the faithful nuclear segregation [14,25], the stable spindle localization near the septin ring inside the daughter bud [16] (Fig. 1(a), Fig. S1 in the Supplemental Material [19], Movie M1 in the Supplemental Material [19]) poses a natural question: what are the force balance conditions necessary for such localization?

In experiments, it is challenging to quantitatively estimate or tweak forces on the spindle in *C. neoformans*. Thus, modeling has been used to supplement and explain the experiments concerning various aspects of spindle mechanics [16,26–34]. Previously, force balance models have been used to replicate the observed aspects of spindle dynamics [35–38]. The "closest to experiment" approach would be to design simulation using an agent-based model [14,16,28,30,33,34,39], where all objects (e.g., MTs, motors, and other organelles) are

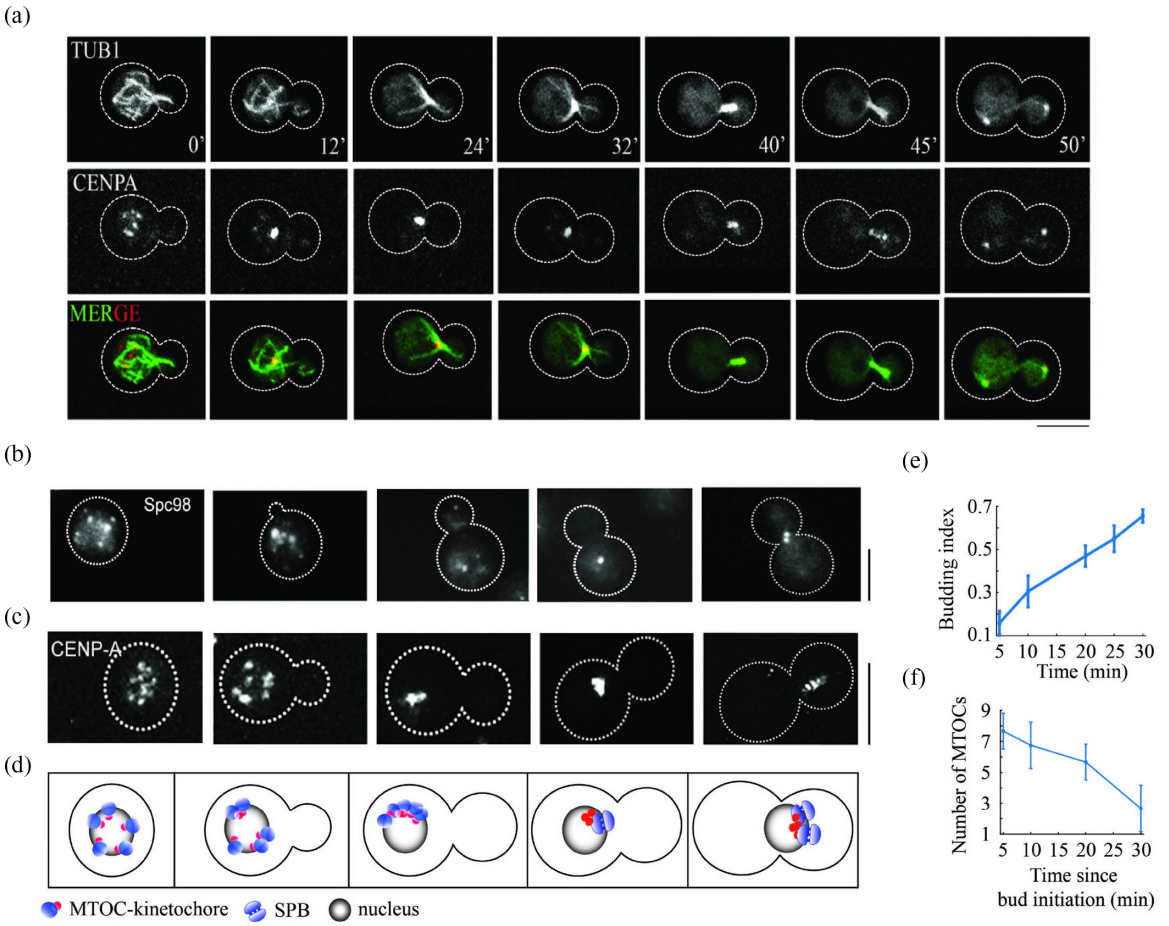

FIG. 1. Cell cycle stages in *C. neoformans* wild-type cell as observed from live-cell imaging. (a) Time series snapshots showing the localization of MTs (GFP-Tub1, depicted in green in the MERGE panel) and KTs (mCherry-CENP-A, depicted in red in the MERGE panel) at different stages of the cell cycle in a wild-type cell. The cell was subjected to time-lapse video microscopy for 60 min. The timestamp (in min) for each image is annotated in the uppermost TUB1 panel. Bar, 5 μm. (b), (c) Clustering of MTOCs and KTs during mitosis in *C. neoformans*. Images of cells showing the localization of (b) Spindle pole body protein, Spc98 and (c) KT marker CENP-A at different cell cycle stages in the wild-type cells. Bar, 5 μm. The snapshots of the co-localization of Spc98 and CENP-A (using a different strain) were shown in Ref. [20]. (d) Schematic depicting the simultaneous happening of the processes shown in panels (b) and (c). (e) Progression of bud growth with time. (f) Number of MTOCs in the cell as a function of time estimated from the bud size.

simulated as agents having their movements dictated by laws of mechanics.

In this study, we utilized an agent-based model with MTs, MTOCs, and nucleus simulated as agents obeying laws of mechanics within a typical budded cell geometry [Fig. 2(a)] [14,16]. Despite the enormous advantages of such an agent-based model, it has certain limitations. In general, the possible number of molecular motors' combinations in various locations of the spindle at different cell cycle stages is too great (discussed in Ref. [40]) and far from clear, particularly in *C. neoformans*. The exact mechanics of the collective motor activity is significantly complex and yet to be well understood. Therefore, for simplicity, we chose not to simulate the molecular motors explicitly. Instead, we opted for a description with constant motor densities where a particular motor-driven force on an MT is proportional to the predetermined motor density. To better understand the spindle positioning, we also set up a simple one-dimensional analytical model with closed-form expressions for various averaged forces [Figs. 2(b) and 2(c)]. By screening these forces, we estimate the plausible force balance for proper spindle positioning in confinement, mimicking a budded cell [23,35,41]. These two models not only complement the primary experimental observations of spindle localization in *C. neoformans*, but reasonably qualitatively corroborates with each other. In other words, the benchmarking of the analytical model is supported by the agent-based model and vice versa. Overall, our study highlights that several mechanistic processes can facilitate efficient clustering of MTOCs, either independently or in harness with the other. Furthermore, screening the outputs of *in silico* models uncovers that proper spindle positioning near the septin ring requires MT buckling from the cell cortex in *C. neoformans*.

II. MODELING METHODS

A. Computational modeling

We consider the spindle dynamics occurring inside cellular confinement mimicking a budded cell [Fig. 2(a)]. The mother bud size (radius R_M) is fixed, whereas the daughter bud (radius r_D) grows with time. Prior to the SPB formation,

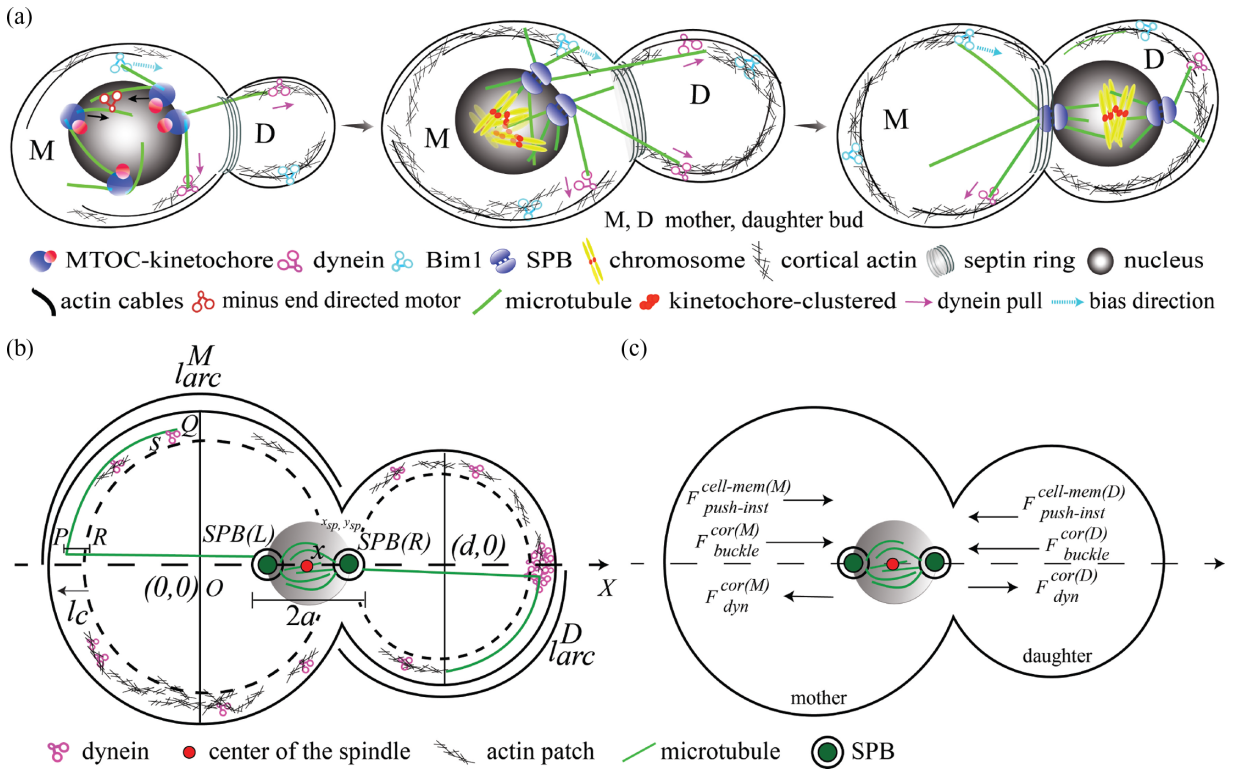

FIG. 2. Representative schematic diagrams illustrating the computational and mathematical model. (a) Model schematic depicts the cell cycle stages in *C. neoformans* which are simulated utilizing the computational model. Plausible interactions of cMTs with the cell cortex and on the nuclear envelope are shown. Arrows indicate the direction of forces. (b) Schematic of the one-dimensional mathematical model for spindle positioning in *C. neoformans*. The origin $O(0,0)$ is located at the center of the mother bud, while the center of the daughter bud is located on the axis of symmetry (namely the X axis) at $(d,0)$. The instantaneous position of the spindle is denoted by x measured from the origin. l_c denotes the cortex's width, filled with mesh-like actins and dyneins. $SPB(L)$ and $SPB(R)$ denote the leftward and rightward SPBs, and the green lines represent microtubules. In the mother bud, the section "PR" is the "uncurled" MT segment in the cortical region, and the segment "PQ" is the "curled" MT segment undergoing sliding within the mother cortex where cortical dyneins pull on both the segments. A similar interaction occurs in the daughter cortex as well. Localized cortical dynein patch in the daughter cortex around the axis of symmetry signifies the differential spatial distribution of dynein in the mother and daughter bud [16]. (c) The direction of the forces acting on the spindle in the mathematical model.

all the MTOCs (spheres of radii $r_{\mathrm{MTOC}} \sim 0.1\,\mu$m) are located on the surface of the outer NE (nondeforming spherical nucleus of radius r_{nuc}) and nucleate cMTs. The movement of the MTOCs is constrained on the surface of the NE. At the onset of the simulation, we considered 14 MTOCs [16,21]. Our previous studies also highlighted the presence of 14 KTs in *C. neoformans* [14,16]. In the model, we considered that at the onset of the bud initiation, KTs are connected to MTOCs. Since the kinetochores are attached to the MTOCs throughout the entire clustering process, it is reasonable to choose the number of MTOCs the same as the number of KTs at the onset of simulation [14,16]. Thus, we have chosen 14 MTOCs in the beginning assuming that each MTOC is associated with a single KT (unless mentioned otherwise). Each MT is modeled as a cylinder of zero thickness with its length regulated by four dynamic instability parameters (Table S2 in the Supplemental Material [19]): catastrophe and rescue frequency (f_c, f_r); growth and shrinkage velocity (v_g, v_s). After complete clustering of MTOCs into the SPB and SPB duplication [Figs. 1(b)–1(f), 2(a)], the nMTs from both the SPBs grow inside the chromosomal volume and capture KTs. Meanwhile, the cMTs that reach the cell cortex, majorly experience instantaneous cortical push ($\vec{F}^{\text{cell-mem}}_{\text{push-inst}}$), push due to buckling against cell membrane ($\vec{F}^{\text{buckle}}_{\text{cor}}$), cortical dynein mediated pull ($\vec{F}^{\text{dyn}}_{\text{cor}}$) and Bim1 mediated bias toward septin ring ($\vec{F}^{\text{Bim1}}_{\text{cor}}$) (Figs. 2(a) and S2(A)–S2(C) in the Supplemental Material [19]). The origin and the direction of these MT-based forces' are summarized in Table II. Previous study [42] shows that the partial rescue of the Bim1△ filament phenotype is consistent with the observations in *S. cerevisiae* and supports the hypothesis that Bim1 acts on the MT cytoskeleton in *C. neoformans*. To that effect, we noted the effective bias toward the septin ring as Bim1 mediated bias/force. Further, the cMTs grazing along the NE experience additional forces (Figs. S2(D) and S2(E) in the Supplemental Material [19]); one of them is $\vec{f}_{\text{overlap}}$ at the MT-MT overlap on NE. The $\vec{f}_{\text{overlap}}$ is proportional to the mean number of minus end-directed motors per unit length (λ_{ovl}) at the overlap (Fig. S2(E) in the Supplemental Material [19]). Similarly, forces between KTs and nMTs have been computed (see the Supplemental Material [19]). The instantaneous positions of all the objects (nucleus, MTOCs, SPBs, KTs) are updated by solving corresponding Stokes equations (Eqs. (S1)–(S4) in the Supplemental Material

TABLE II. Description of MT-based forces present in the *in silico* model.

Forces	Origin	Direction
Instantaneous push ($F^{\text{cell-mem}}_{\text{push-inst}}$)	MT tip hitting the cell wall	Directed along the MT, away from the cell wall
Dynein mediated cortical pull ($F^{\text{cor}}_{\text{dyn}}$)	MT sliding in cell cortex	Directed along the MT, toward the cell cortex
Bim1 bias ($F^{\text{cor}}_{\text{Bim1}}$)	Cortical sliding of MTs toward septin ring	Directed toward the septin ring
MT buckling ($F^{\text{cor}}_{\text{buckle}}$)	MTs impinged on the cell boundary	Directed along the MT, away from the cell cortex
Inter-cMT coupling	Overlapping antiparallel MTs grazing the NE	Directed along the MT, away from the cell cortex
Push due to MT polymerization in cortex ($f^{\text{MT-poly}}_{\text{cor}}$)	Cortical resistance on polymerizing MT tip	Directed along the MT, away from the cell cortex
Force at ipMT- ipMT overlap (f_{ipMT})	Collective activity of kinesin-5 motors at ipMT-ipMT overlap	Directed along the MT, leading to the separation of the SPBs
Push by growing kMTs ($f^{\text{growth}}_{\text{push}}$)	kMT tip penetrating into the KT	Directed along the MT, away from the KT
Pull by shrinking kMTs ($f^{\text{shrinkage}}_{\text{pull}}$)	Separation between kMT tip and KT	Directed along the MT, pulling the KT

[19]). The detailed simulation procedure is described in the Supplemental Material [19]. In the following, we briefly outline the simulation algorithm in a step-by-step fashion.

(1) To begin with, we modeled the budding yeast cell confinement as the union of two unequal intersecting spheres. One sphere represents the mother bud (radius R_M) and the other one, the daughter bud (radius r_D). In simulations, the radius r_D is gradually increased with time to replicate the bud growth as observed on experiments. In the model, the circle spanned at the intersection of the two spheres is mapped as the septin ring of the *real* cell. (2) The nucleus is considered as a sphere of radius r_{nuc}.

(3) The cell cortex is marked as a layer of finite width l_c underneath the spherical cell boundary.

(4) Next, we modeled the MTs as semiflexible polymers with their length being regulated by dynamic instability [43,44].

(5) In the next step, we modeled MTOCs as spherical objects with fixed radius on the outer NE (surface of the spherical nucleus with radius r_{nuc}). The movement of the MTOCs is strictly constrained on this outer surface of the nucleus. Similar to the MTOCs, the SPBs are also modeled as rigid spheres (radius r_{SPB}) embedded on the NE.

(6) The KTs are also modeled as spheres, with the sister KTs connected via a Hookean spring. This connection mimics the cohesin linkage between the sister KTs.

(7) Next, we simulate the cMT-cell cortex interaction and the inter cMT coupling at the NE by framing a myriad of MT-based forces in the *in silico* setup. The major interactions considered in the model are listed below: (a) instantaneous push $F^{\text{cell-mem}}_{\text{push-inst}}$—the instantaneous force exerted on the MT tip upon each encounter with the cell boundary, (b) cortical pull $F^{\text{cor}}_{\text{dyn}}$—force due to dynein pull on the MTs sliding inside the cell cortex, (c) Bim1 bias $F^{\text{cor}}_{\text{Bim1}}$—directed force bias (expected to be facilitated by Bim1 protein complex along with other regulating factors) exerted on the cMTs inside the mother cell cortex toward the septin ring, (d) MT buckling $F^{\text{cor}}_{\text{buckle}}$—force stemming from MT buckling transition [45,46] at the cell boundary, (e) inter cMT coupling on NE- force originating at antiparallel cMT-cMT overlap near NE due to minus end-directed motor activity. Similarly, the nMT-KT interactions are also modeled. The detailed description of all the forces considered in the model and how they are implemented in the simulations are discussed in the Supplemental Material [19].

(8) At each time step, net resultant force on each object (e.g. MT, MTOC, SPB, KT, nucleus, etc.) is calculated through the vectorial sum over the individual forces acting on the object under consideration. Next, we frame and subsequently solve the equations of motion to simulate the spatiotemporal dynamics of the nucleus, MTOCs, KTs and SPBs.

1. Equations of motions dictating the spatiotemporal dynamics of the nucleus, MTOCs, kinetochores, SPBs

When a cMT interacts with the cortex, a force due to the cortical interaction is transduced via the cMT and exerted on the nucleus and the MTOCs/SPBs simultaneously. In addition to that, the force due to the ipMT interaction also acts on the SPBs. If $\vec{F}_{\text{nucleus}}$, $\vec{F}_{\text{MTOC}}$, and $\vec{F}_{\text{SPB}}$ are the net resultant forces exerted on the nucleus, MTOC, and SPB, respectively, then the corresponding equations of motion can be written as

$$\frac{d\vec{R}_{\text{nucleus}}}{dt} = \frac{\vec{F}_{\text{nucleus}}}{\zeta_{\text{nucleus}}}, \tag{1}$$

$$\frac{d\vec{R}_{\text{MTOC}}}{dt} = \frac{\vec{F}_{\text{MTOC}}}{\zeta_{\text{MTOC}}}, \tag{2}$$

$$\frac{d\vec{R}_{\text{SPB}}}{dt} = \frac{\vec{F}_{\text{SPB}}}{\zeta_{\text{SPB}}}, \tag{3}$$

where $\vec{R}_{\text{nucleus}}$, $\vec{R}_{\text{MTOC}}$, and $\vec{R}_{\text{SPB}}$ represent the instantaneous positions of the nucleus, MTOCs, and SPBs, respectively, at a certain time step. ζ_{nucleus}, ζ_{MTOC}, and ζ_{SPB} denote the viscous drag on the corresponding objects. $\vec{F}_{\text{nucleus}}$, $\vec{F}_{\text{MTOC}}$, and $\vec{F}_{\text{SPB}}$ contain vectorial contributions from $\vec{F}_{\text{cor}}^{\text{MT-poly}}$, $\vec{F}_{\text{push-inst}}^{\text{cell-mem}}$, $\vec{F}_{\text{dyn}}^{\text{cor}}$, and $\vec{F}_{\text{buckle}}^{\text{cor}}$. The net force on an MTOC $\vec{F}_{\text{MTOC}}$ is divided into two components: (a) tangential to the NE and (b) normal to the NE. As the movement of MTOC is considered constrained on NE, only the tangential force component is responsible for moving the MTOC on NE, the normal component is not allowed to contribute to the motion of MTOCs confined at the NE. The same procedure applies to the motion of the SPBs as well, as the SPBs are taken to be embedded on the NE throughout the mitotic period considered in the simulation. Due to the attachment of the MTOCs with the surface of the NE, the resultant force on the nucleus can be computed as the vectorial sum over the net cortical forces on individual MTOCs.

Similarly, the motion of a KT is governed by the following equation of motion,

$$\frac{d\vec{R}_{\text{kinetochore}}}{dt} = \frac{\vec{F}_{\text{kinetochore}}}{\zeta_{\text{kinetochore}}}. \tag{4}$$

Here, $\vec{R}_{\text{kinetochore}}$, $\vec{F}_{\text{kinetochore}}$, and $\vec{\zeta}_{\text{kinetochore}}$ represent instantaneous position, net force on the KT, and the viscous drag experienced by the KT, respectively. $\vec{F}_{\text{kinetochore}}$ entails a vectorial summation over $\vec{f}_{\text{push}}^{\text{growth}}$, $\vec{f}_{\text{pull}}^{\text{shrinkage}}$, $\vec{f}_{\text{ipMT}}$, $\vec{f}_{\text{cohesin}}$, and $\vec{f}_{\text{intersection}}$. For simplicity, we have not considered contributions of thermal diffusion (Brownian motion) while computing the positional update of any of the objects considered in the model.

The equations of motion are discretized and solved using Euler's method at every time step.

The agent-based stochastic MT dynamics simulation is written in FORTRAN. The data analysis and plotting have been carried out in MATLAB (The MathWorks, Natick, MA) and Gnuplot. A single simulation run takes few minutes of real computation time until a stable spindle positioning is attained starting from MTOC clustering (in Intel Xeon CPU having clock speed 2 GHz, RAM 32 GB).

B. Mathematical modeling

1. *Framework*

We formulated a mathematical model to study spindle positioning. We frame the mother and the daughter bud as two intersecting circles of radii R_M and r_D, respectively (Table S2 in the Supplemental Material [19]). The daughter bud's center is chosen to be d distance away from the mother's center. In this framework, the spindle's spatial movement is allowed along the line joining the centers, regarded as the axis of symmetry. For simplicity, our analytical model is one-dimensional, where all the forces are projected along the axis of symmetry, namely, the X axis [Figs. 2(b) and 2(c)]. The spindle is chosen to be a rigid rod of length $2a$ with two perfectly bioriented SPBs at its ends lying on the X axis. We further assume that the cMTs from the SPB facing the mother (daughter) bud cell cortex, namely SPB(L) [SPB(R)], interact solely with the mother (daughter) bud cell cortex [Figs. 2(b) and 2(c)]. In the following, we discuss the reasons behind these assumptions. The spindle is nearly aligned with the axis joining the mother and daughter bud center [Fig. 1(a)]. The geometric obstruction imposed by the solid nucleus, the relatively smaller aperture of the bud-neck junction, and the spindle alignment parallel to the axis joining the mother and daughter bud center prevent the cMTs from an SPB to interact with both mother and daughter bud cell cortex in an isotropic manner. The cMTs emanating from the SPB facing the mother (daughter) bud cell cortex majorly interacts with the mother (daughter) cell cortex only [Fig. 2(a)].

Further, in the model, we considered exponentially decaying spatial dependence of forces, a straightforward and widely used choice [23,35,41]. We derived closed-form expressions for various MT-mediated forces (instantaneous cortical push, cortical dynein pull, the force due to MT buckling) on the spindle due to MT-cell cortex interaction. The sum of all these forces accounts for the total force on the spindle. The net force balance on the spindle [rigid rod constituting SPB(L) and SPB(R)] determines the spindle position.

Here, the strength of dynein-mediated pulling is regulated by λ_{dyn}^{M} (Eqs. (S7) and (S8) in the Supplemental Material [19]) and λ_{dyn}^{D} (Eqs. (S10) and (S11) in the Supplemental Material [19]), cortical pushing by A_M and A_D (Eqs. (S5) and (S6) in the Supplemental Material [19]), average MT length by $L_{\text{MT}}^{\text{av}}$ (Eqs. (S5)– (S8), Eqs. (S10) and (S11), Eqs. (S13) and (S14) in the Supplemental Material [19]). In the numerical simulation, the corresponding model parameters are adjusted according to the values listed in Table S2 in the Supplemental Material [19]. In most cases, the choice of the parameter values is based on the earlier published reports. However, due to the paucity of exact numbers in the literature, a few of the chosen parameter values are optimized for the current study through sensitivity analysis.

2. *Utility*

In wild-type cells, after SPB separation close to the septin ring, we observe stable spindle localization inside the daughter bud, parallel to the axis joining the center of the mother and daughter bud. This stable localization naturally results from a mechanical force balance within the cellular confinement governed by MTs and molecular motors. Rather than presuming a force balance landscape that supports this localization, we begin by utilizing the simplistic analytical model to screen various forces and determine which combinations of forces are responsible for replicating the qualitative features of the observed phenotypes. Furthermore, closed-form force expressions elucidate the subtle force characteristics of spindle positioning from a primarily mechanistic perspective. Taking a cue from this analytical screening of forces, we "feed" the learned force combinations into a detailed agent-based model with explicit simulations of stochastic MT dynamics and MT interactions with the cell cortex to validate the lessons from the analytical model screen. It is natural to ask why we consider the one-dimensional model when the three-dimensional model presumably tells us more? The reasons are: (a) to have a first-hand understanding of steady-state characteristics due to force balance when the spindle is placed near the septin ring

from a minimal model and (b) to quickly screen the combinatory effect of various forces on spindle positioning. Therefore, we reiterate that it is beyond the scope of the one-dimensional model to investigate the dynamics of the spindle positioning; we have a three-dimensional agent-based model to serve that purpose. The mathematical model is described in detail in the Supplemental Material [19]. In the following, we present the model investigations exploring MTOC clustering and spindle positioning in *C. neoformans*.

3. Analytical model assumptions and comparisons with the agent-based model

The mathematical model construction is based upon several simplifications described in the following: (1) The model does not account for the process of biorientation on the NE. We assume a bioriented configuration of two SPBs throughout [Figs. 2(b) and 2(c)]. In the agent-based model, after SPB duplication, the process of SPB biorientation has been taken into account. (2) In the analytical model, the spindle length is fixed independent of its position along the axis of symmetry. In the agent-based simulations, spindle length is determined by the forces acting on nMTs and cMTs. (3) In the one-dimensional analytical model, the motion of the nucleus and spindle is strictly confined along the X axis. We only emphasize the translational motion of the spindle governed by a set of MT-mediated forces. The rotational degrees of freedom responsible for the spindle orientation is not considered in the model for simplicity. The spindle is always laid upon the X axis, with its orientation being parallel to the symmetry axis (X axis). Allowing the spindle to move only along the X axis accounts for the net cancellation of forces along the transverse direction since MT nucleation is considered isotropic in all directions. In the agent-based model, simulated on a three-dimensional geometry, no such restrictions have been imposed [Figs. 2(a)–2(c)]. (4) The analytical model does not include stochastic fluctuations originating from the randomness in MT dynamics or its interaction with the cell cortex. The closed-form expressions of the governing forces are evaluated in a time-independent quasi-equilibrium configuration. In the agent-based model, a significant source of stochastic fluctuations is the MT dynamic instability [1,43,44,47] and attachment and detachment of molecular motors. (5) For simplicity, we have not considered a load-dependent variation of average MT length in the analytical model. However, in the agent-based simulation, load-dependent modulation of the MT dynamic instability parameters, growth velocity (v_g), and catastrophe frequency (f_c) have been taken into account.

The experimental protocol is described in the Supplemental Material [19].

III. RESULTS

A. Clustering of MTOCs progresses via redundant pathways

We have shown previously that all KTs cluster to form a punctum in ∼25 min [16]. We further demonstrated that KTs colocalize with MTOCs [20]. Now, we validated the time required for MTOCs to coalesce into an SPB by calibrating the clustering time since bud initiation (time set to zero), in terms of the budding index [Figs. 1(e) and 1(f)]. Since the bud initiation, the daughter bud grows with time in a reasonably uniform manner over a large population of cells. As the bud growth rate is roughly consistent, the budding index can be considered an intrinsic "clock" of a budded cell [Fig. 1(e)]. The number of MTOCs in cells having similar budding indices (implying that the cells are at the same cell cycle stage) was counted and plotted with "time" (calibrated from the budding index) to estimate the MTOC clustering time [Fig. 1(f)]. Note that while measuring the absolute time, rather than calculating it from the bud size, would be more appropriate for studying the course of MTOC clustering, the present manuscript aimed to understand the plausible mechanisms of MTOC clustering from the estimate of average clustering time. Since unclustered and clustered MTOCs occur at two endpoints of the measurements, the time difference between these events estimated from several bud-size measurements was consistent.

We observed that the timescale for KT clustering [16] and MTOC clustering [Fig. 1(f)] are similar (∼25 min) and in good synchrony with each other [Figs. 1(a)–1(d)]. Although electron microscopy suggested as many as 14–16 MTOCs [21], with a limited resolution, we could identify a maximum of 8–10 MTOCs in small budded cells. Next, we address how all the MTOCs cluster into a single group within this specific timescale using an agent-based mechanistic model (Figs. 2(a), 3(a) and Fig. S2 in the Supplemental Material [19]). First, we investigated the MTOC clustering process via MT-driven "search and capture" on the NE without the cortical interactions (Fig. 3(a) and Fig. S2(D) and S2(E) in the Supplemental Material [19]). First, we determined the time required for all the MTOCs to cluster if cMTs growing out of MTOCs slide along the NE and directly capture the MTOCs (Fig. S2(D) in the Supplemental Material [19]). We considered that in the "direct search and capture" mechanism (Fig. 3(a) and Fig. S2(D) in the Supplemental Material [19]), the MTs contributing to the clustering process remain confined to the NE while growing in a random direction. As the "searcher" MT tip nucleated from an MTOC grazes along the NE and "captures" another MTOC ("target"), the MTOCs move toward each other along the MT until they fuse (Fig. 3(a) and Fig. S2(D) in the Supplemental Material [19]). The movement of the MTOCs is strictly restricted to the NE. In this context, we assumed a fixed number of grazing cMTs per MTOC (∼3–4 cMTs per MTOC). We found that the timescale for complete clustering achieved by this "direct search and capture" pathway is significantly large, surpassing the relevant mitotic timescales in the explored parameter regime. The MTOCs take ∼1.5 h to cluster entirely, that too, in ∼10% of the cell population only. The MTOCs fail to cluster into a single focus in the rest of the cell population even after ∼4–5 h. Note that, in the current *in silico* study, the term "cell population" alludes to the total number of independent simulation runs started with uncorrelated initial configurations. In this particular context, we performed many separate simulation runs, and in 10% of these simulations, clustering less than 1.5 h was observed. Thus, it is unlikely to be an "efficient" pathway for MTOC clustering in the currently explored parameter regime. However, the possibility that the same pathway functioning efficiently in combination with other pathways cannot be ruled out.

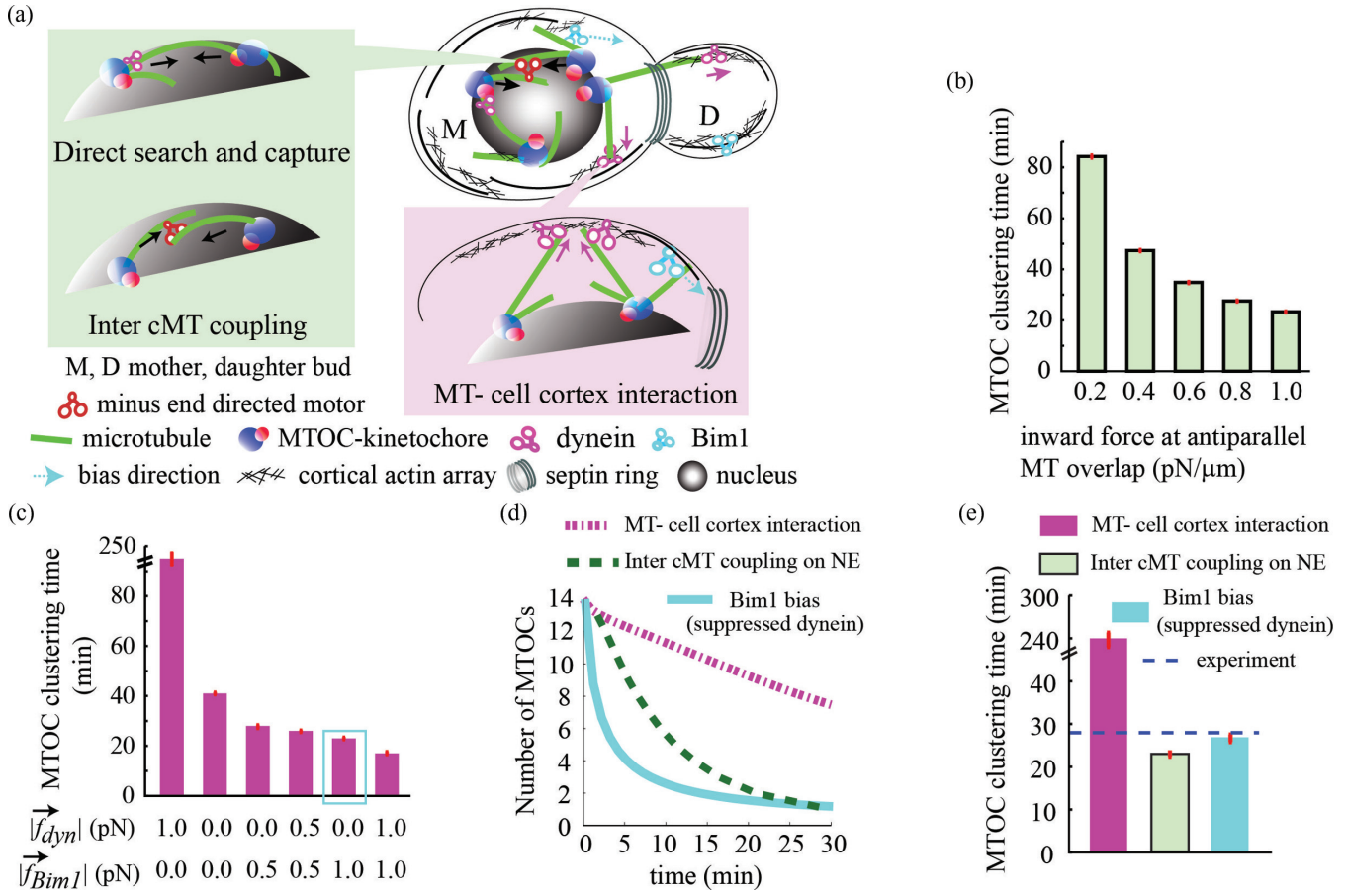

FIG. 3. Cooperative interactions among MTs and motors govern MTOC clustering. (a) Model schematic depicting MT-mediated 'search and capture' processes and forces required for the clustering of MTOCs. Arrows indicate the direction of forces. Plausible clustering mechanisms illustrated are: a growing cMT directly capturing an MTOC ('direct search and capture'), sliding of antiparallel cMTs via crosslinking minus end-directed motors on the NE (inter cMT coupling at the NE), and cMT plus-ends interacting with cell cortex (MT-cortex interaction). (b) Clustering time in the sole presence of inter cMT coupling at the NE increases as the minus-ended motor-generated inward force at MT-MT overlap decreases. The MT number is fixed at 4 per MTOC. (c) Clustering solely via MT-cell cortex interaction. The clustering is faster when the Bim1 bias is enhanced. $|\vec{f}_{\rm dyn}|$ ($|\vec{f}_{\rm Bim1}|$) represents the magnitude of the force generated by a single dynein (Bim1) on each MT at mother cortex. (d) Time progression of MTOC clustering in different mechanisms. The first/fifth bar in part (c) denotes the parameter values corresponding to the magenta/cyan curve in part (d), respectively. (e) Comparison between MTOC clustering timescales via MT-cell cortex interaction, inter cMT coupling on NE and Bim1 bias with suppressed dynein activity at cell cortex ($|\vec{f}_{\rm dyn}| = 0.0$ pN, $|\vec{f}_{\rm Bim1}| = 0.5$ pN). In all figures, sample size $n > 2000$ for simulation and red bars indicate SEM (wherever shown).

Next, we introduced antiparallel sliding amongst the grazing cMTs on the NE (inter-cMT coupling, Fig. 3(a) and Fig. S2(E) in the Supplemental Material [19]). Inward sliding of the overlapping cMTs from two different MTOCs can be steered by crosslinking minus end-directed motors [48]. The crosslinking activity of minus end-directed motors acting at the MT-MT overlap brings the engaged MTOCs toward each other. In the earlier scenario, a "searcher" MT has to grow and capture another MTOC. However, in the present context, a "searcher" MT can grow and capture another MT segment so that the minus end-directed motors can crosslink them and initiate antiparallel sliding. Adding the minus end-directed motor crosslinking and sliding on the NE facilitate the timely clustering; clustering of all the MTOCs (∼100%) into a single object happens within ∼23 min (Fig. 3(b) and Movie M2 in the Supplemental Material [19]). As expected, when the inward force between the MTOCs due to minus-ended motors diminishes, the net clustering time increases [Fig. 3(b)]. Additional parameter sensitivity analysis for this clustering mechanism is described in Fig. S3 in the Supplemental Material [19].

In essence, the modeling results propose the "minus end-directed motor mediated antiparallel cMT sliding on NE" as a plausible mechanism of MTOC clustering within the experimentally observed time window. A possible candidate for this process is minus-ended dynein. Hence, we experimentally tested whether dyneins are present on NE during MTOC clustering. To this note, the dual-color imaging of Dyn1 and MTOCs will strengthen the case of theoretically proposed minus-end directed motor-mediated coupling and sliding of antiparallel cMTs. However, it is technically challenging to address this where we have to construct a strain where either Dyn1 and MTOCs or Dyn1 and MTs are tagged simultaneously due to the limited availability of auxotrophic markers in this organism. Instead, we expressed GFP-tagged Dyn1 and studied its relative localization with respect to the

nuclear periphery protein Sad1-mCherry. We have shown previously that Sad1 localizes to the nuclear periphery and the dot-like signal of Sad1 is only restricted to the NE [20]. Sad1 also connects kinetochores to the MTs/MTOCs and facilitates clustering. We observed multiple dynein puncta surrounding the nuclear periphery (Fig. S12 in the Supplemental Material [19]). Occasionally, dynein partially colocalizes with Sad1 (Fig. S12 in the Supplemental Material [19]), indicating that Dyn1 might be involved in the sliding of cMTs. Since some signals from Dyn1 were weakly detected, we could not quantify the exact number of dynein molecules in this strain. Note that, at this stage, the presence of any other minus-end directed motor candidate (besides dynein) cannot be ruled out (therefore, testing the role of other minus-end directed motor candidates, e.g., kinesin-14 in MTOC clustering is a worthy future venture).

Next, in the model, we explore the role of cMT-cell cortex interaction leading to the clustering of the MTOCs. Two major cortex-based forces on the cMTs are: (a) net pull on the MT segments sliding inside the cortex via the cortical dyneins toward the cortex; (b) Bim1 mediated force on the cMTs (sliding +ve end of the cMTs along the cortex) having a directional preference towards the septin ring (MT-cell cortex interaction, Fig. 3(a) and Figs. S2(A) and S2(B) in the Supplemental Material [19]). We found that the exclusive activity of dynein-mediated MT-cell cortex interaction leads to nearly complete clustering of the MTOCs, but the time estimated ($\sim$240 min) is way too high (Fig. 3(c) and Movie M3 in the Supplemental Material [19]). However, a decrease in the cortical pull and/or subsequent increase in the Bim1 mediated bias reduces the clustering timescale to $\lesssim$50 min (Figs. 3(c), 3(d) and Movie M4 in the Supplemental Material [19]). We find that the dynein-mediated pull on the MTOCs via cMTs acts in random directions, whereas the Bim1 mediated bias is directed towards the septin ring. Thus, dynein dominated cortical pull suppresses the effective Bim1-bias and delays the clustering. When dyneins are suppressed, due to Bim1-bias, all the MTOCs are drifted toward the septin ring along the NE and cluster rapidly. Note that if the clustering time via a mechanism largely exceeds the physiological time limit estimated from the live-cell imaging, the sole presence of the mechanism under consideration may be discarded. In reality, significantly delayed clustering by any 'inefficient' mechanism is unlikely to happen in the context of a dividing cell.

The timescales for complete MTOC clustering appears to be similar and close to the physiological time limit when (a) MTOCs aggregate due to antiparallel sliding of the grazing MTs on the NE via minus ended motors and (b) MTOCs aggregate due to diminished cortical dynein pull concomitantly with enhanced Bim1-bias at the cortex (Figs. 3(d), 3(e) and Table S3 in the Supplemental Material [19]). This highlights a crucial physical possibility that the clustering mechanisms may be redundant, i.e., the mechanisms either act in liaison or independently. Note that in our microscopic images, owing to the limited resolution, we were able to recognize a maximum of 8–10 MTOCs in small budded cells. However, in simulations, we considered 14 MTOCs. Due to this difference in MTOC number, we observe discrepancies in the time progression of MTOC clustering if we compare the corresponding experimental data with simulations [Figs. 1(f) and 3(d)].

The complete clustering of MTOCs into a single body marks the formation of the mature SPB followed by SPB duplication. Subsequently, the duplicated SPBs separate into a bioriented configuration that initiates spindle formation. In our earlier and present studies, it has been shown that the mitotic spindle stabilizes inside the daughter bud close to the septin ring in *C. neoformans* [16] [Fig. 1(a), Movie M1 in the Supplemental Material [19], Fig. 2(a)].

Therefore, an obvious precursor to the spindle positioning inside the daughter bud is nuclear migration from the mother bud to the daughter. From a mechanistic standpoint, this is facilitated by cortical interaction of cMTs (Fig. 2(a), Figs. S2(A)– S2(C) in the Supplemental Material [19]) [14,16]. Interestingly, cortical interaction is also an important mode of MTOC clustering, as we have already shown. Therefore, MTOC clustering, nuclear migration, and subsequent spindle positioning are the sequence of crucial mitotic events that are unlikely to be mutually exclusive. The key elements necessary for orchestrating the pre-anaphase MTOC clustering and nuclear migration are (a) MT integrity and (b) spatiotemporal localization and activity of Bim1 and dynein [16]. Bim1 and dynein majorly generate the forces transduced via cMTs to the MTOCs (later SPBs) and the nucleus.

Previously, we showed that Aurora B kinase Ipl1 in *C. neoformans* plays a pivotal role in (a) maintaining MT stability and (b) regulating Bim1-dynein activity or localization [16]. The depletion of Ipl1 interrupts both MT stability and Bim1-dynein activity. We observed that delayed KT clustering correlates with delayed nuclear migration among heterogeneous phenotypes of defective KT clustering and impaired nuclear migration in Ipl1 depleted cells. Since the timescales of MTOC clustering and KT clustering are similar and occur concomitantly [16] [Figs. 1(b)–1(f)], it is likely that delay in MTOC clustering also leads to a delay in nuclear migration.

Taking cues from these experimental observations, we asked the following questions in the *in silico* model: (a) What happens to the nuclear migration and concomitantly progressing MTOC clustering when cortical Bim1 and dynein densities are varied? Note that, "density" of molecular motors and "force" applied by them are proportional in our model. Thus, variations in the Bim1 and dynein densities allude to equivalent variations in the respective forces. (b) Does impaired or delayed clustering lead to faulty migration? (c) What happens to the spindle positioning and spindle orientation when MTOC clustering is delayed?

To address these questions, we carried out sensitivity analysis over the following parameters: Bim1 bias force per MT, the number of MT per MTOC, and average cMT length (Figs. 4(a)–4(c) and Figs. S5(A) and S5(B) in the Supplemental Material [19]). We find that the time required for MTOC clustering and nuclear migration are reasonably correlated. If the MTOC clustering is delayed or accelerated, then nuclear migration also follows a proportional timescale [Figs. 4(a)–4(c)] [16].

Furthermore, a close inspection of Fig. 1(a) indicates that the mother bud also appears to grow over time, albeit at a much slower speed. We numerically assessed whether this small change in the mother bud size with time affects the

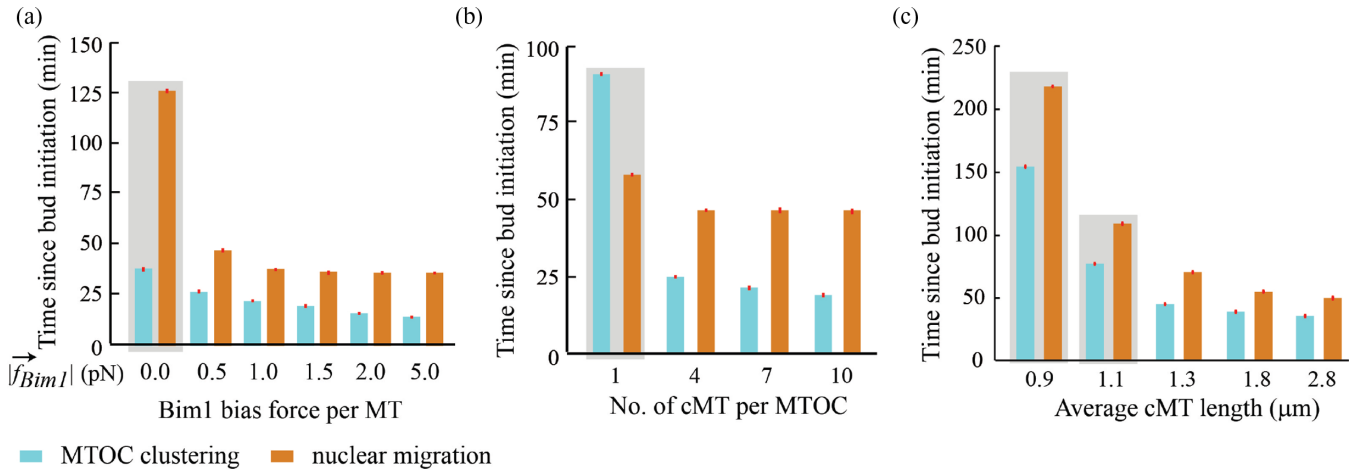

FIG. 4. MTOC clustering and nuclear migration: sensitivity to model parameters. (a)–(c) Time required for complete MTOC clustering and proper nuclear migration to daughter bud when Bim1 bias force per MT (a), number of MT per MTOC (b), and average cMT length (c) are varied. For MTOC clustering, solely the mechanism of "MT-cell cortex interaction with diminished cortical pull and enhanced Bim1 bias" is considered. In all figures, sample size $n > 2000$ for simulation and red bars indicate SEM (wherever shown).

timescales of MTOC clustering and nuclear migration. To this note, we have performed several simulations where the mother bud also grows with time in harmony with the daughter bud. In our simulations, we begin with a particular radius of the mother bud. The radius increases with time until it reaches a fixed, predetermined value. Quite evidently, in the simulations, the mother bud's growth rate is considered to be much slower than that of the daughter bud. In the currently explored parameter regime, we do not observe any significant change in MTOC clustering and nuclear migration time when the feature of mother bud growth over time is introduced in the model (Fig. S11 in the Supplemental Material [19]). Therefore, it is reasonable to keep the mother bud at a fixed size throughout the simulations (unless mentioned otherwise).

Interestingly, the *in silico* analysis further suggests that the delay in nuclear migration and MTOC clustering do not affect the spindle positioning or the spindle orientation in the currently explored parameter regime (Figs. S5(A) and S5(B) in the Supplemental Material [19]). Variations in Bim1 bias force per MT and the number of MT per MTOC incur variations in the nuclear migration time (and MTOC clustering time) within a reasonable range [Figs. 4(a)–4(c)]. But the spindle positioning within the daughter bud (and spindle orientation) turns out to be independent of the variations in Bim1 bias force per MT and number of MT per MTOC (Figs. S5(A) and S5(B) in the Supplemental Material [19]). In other words, irrespective of whether the nuclear migration is delayed or accelerated, the stable spindle position (and spindle orientation) remain unchanged within this specific cellular geometry (Figs. S5(A) and S5(B) in the Supplemental Material [19]). Experimental quantification of various spindle attributes in wild-type and upon molecular perturbations (Figs. S1, S4(A)–S4(C), S5(C)–S5(E), and S6 in the Supplemental Material [19]) are discussed in the following sections. Additionally, the quantification protocols for the experimental data on nuclear migration are discussed in the Supplemental Material [19] in detail.

To understand the stable spindle localization, we propose a simple analytical model that estimates the net force balance on the spindle [see the Supplemental Material [19] and Figs. 2(b) and 2(c)]. We considered closed-form expressions for various MT-based forces and examined possibilities of the spindle localization under the combinatory effect of these forces (Figs. 2, 5 and Fig. S7 in the Supplemental Material [19]).

B. Balance of cellular mechanical forces guides the spindle position

A spindle is constantly acted upon by molecular forces arising from the interactions of its components with the surrounding [14,16,23,29,34,49–51], e.g., cMTs interacting with the cell cortex via dynein generates a pull on the nucleus toward the cell periphery; similarly, cMTs buckling in contact with the cell membrane pushes the nucleus away from the membrane. These interactions are plausible in both mother and daughter bud cell cortices. Besides, interactions of cMTs with the septin ring and the cortical actin cables generate an effective bias translating the plus ends of the cMTs toward the daughter bud. Since these forces are spatially inhomogeneous and rapidly varying with time, it is logical to ask how the nucleus and the spindle attain steady positions before the chromosomal segregation. As mentioned previously, to elucidate the force balance of spindle positioning, we took resort to the following modeling prescriptions: (a) a simplistic one-dimensional analytical model that deals with closed-form mean-field force expressions for major MT-based forces on the spindle and (b) a detailed three-dimensional agent-based model with MTs and other associated spindle components simulated as agents with a multitude of mechanistic interactions between them. In the following, first, we present the findings from our analytical model of spindle positioning. Next, we describe the agent-based modeling results in the context of the same.

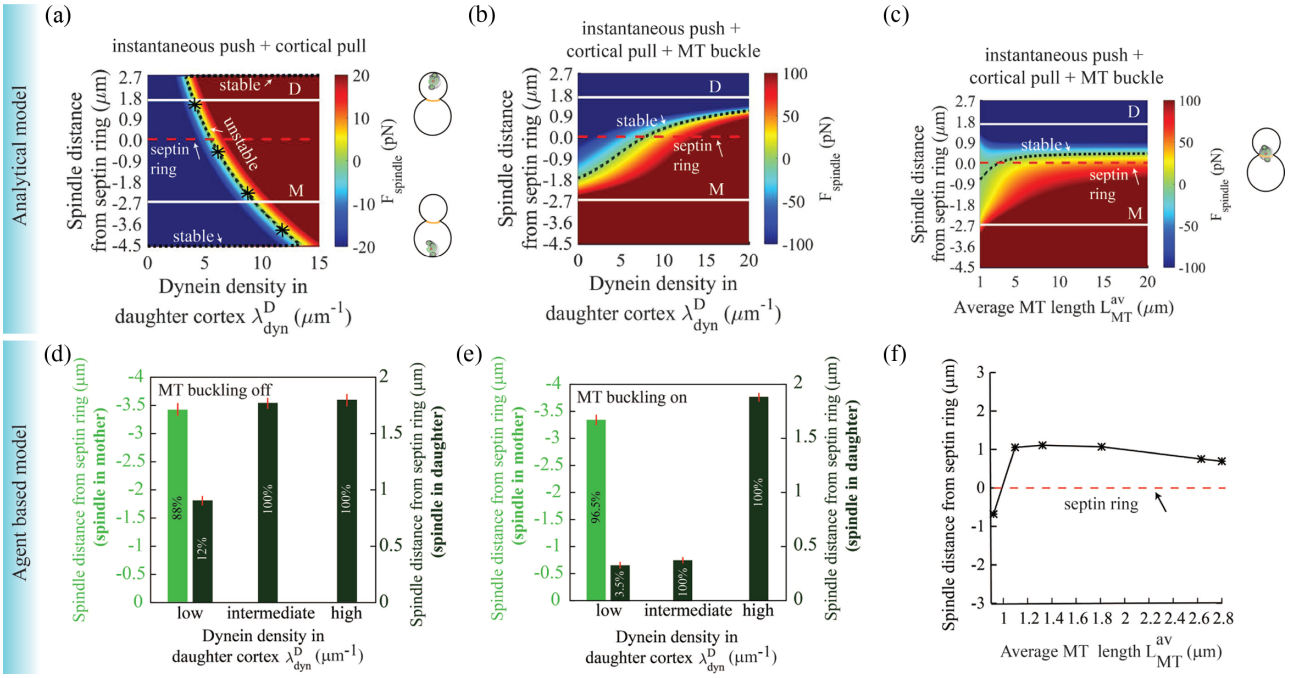

FIG. 5. The mechanistic models of force balance explain spindle positioning in *C. neoformans*. (a) Spindle stably collapses onto the cell cortex as dynein density in the daughter cortex (λ^{D}_{dyn}) is varied. Dynein density in the mother cortex (λ^{M}_{dyn}) is fixed and instantaneous cortical push is present in both mother and daughter cortex. Color bars represent the net force on the spindle and white solid lines denote the center of the daughter and mother buds. (b), (c) MT buckling is present combined with instantaneous push and cortical pull. Increasing dynein density in the daughter cortex (λ^{D}_{dyn}) steadily brings the spindle into the daughter, localizing near the septin ring (b). Spindle position varies depending on the average MT length L^{av}_{MT} (c). (d), (e) Spindle distance from septin ring in the absence (d) or presence (e) of MT buckling at the cortex as observed in the agent-based simulation. The values within the bars indicate the percentage of spindles in mother or daughter across the cell population. (f) Spindle position depending on the variation in average MT length (L^{av}_{MT}) as observed in the agent-based simulation when instantaneous cortical push, dynein pull, and MT buckling are acting in tandem. In plots A–F, -ve/+ve distance refers to the spindle in the mother (M) and daughter (D) bud.

1. Spindle positioning: Analytical model findings

We formulate an analytical template in one dimension that accommodates key MT-mediated forces originating from the mother and daughter cortices acting on the SPBs [Figs. 2(b) and 2(c)]. The mechanistic force balance landscape emerging from the mathematical model allows us to carry out sensitivity analysis across a broad parameter regime constituting a myriad of forces with different characteristics (e.g., instantaneous pushing and buckling of the cMTs, dynein mediated pulling, etc.). From experiments and agent-based simulation, we observe that the average spindle length is $\sim 1.5\,\mu$m in wild-type (Fig. S5(C) in the Supplemental Material [19]) and the neck to spindle distance is $\sim 1\,\mu$m while the spindle is in the daughter bud (Fig. S5(D) in the Supplemental Material [19]). Also, the spindle lies almost parallel to the axis of symmetry (orientation angle $\sim$15 degree), joining the centers of the mother-daughter bud (Fig. S5(E) in the Supplemental Material [19]).

To test how sensitive is the spindle positioning to the cMT-cortex-based forces, we introduced instantaneous push and dynein pull from both the mother and daughter cortex. Then, we varied the daughter cortex's dynein density, keeping the rest of the parameters fixed at base values denoted in Table S2 in the Supplemental Material [19]. If the daughter cortex's dynein pull is too strong, then the spindle collapses onto the daughter cortex. In the other limit, the spindle collapses onto the mother cortex when the mother cortex's pull overpowers the pull from the daughter [Fig. 5(a)]. Thus, in the absence of MT buckling, the spindle localizes at the cortex. Note that the term "collapse" means the spindle is dragged too close to the cell cortex.

Adding the force due to MT buckling (with two other forces: cortical pull and instantaneous push) restores the stable spindle position near the septin ring [Figs. 5(b) and 5(c)]. The spindle robustly maintains its position inside the daughter bud, close to the septin ring upon considerable variation in the average cMT length (Fig. 5(c), Table S4 in the Supplemental Material [19]).

2. Spindle positioning: Agent-based model findings

We also tested the spindle positioning in the absence and presence of MT buckling, utilizing the three-dimensional agent-based computational model [Figs. 5(d) and 5(e)]. We find that a moderate dynein pull is crucial for the spindle to migrate into the daughter. In the absence of MT buckling, the spindle localizes deep inside the daughter cortex for moderate and robust dynein pull from the daughter [Fig. 5(d)]. The nucleus is retained in the mother bud for small dynein pull from the daughter cortex [Fig. 5(d)].

With MT buckling turned "on," the spindle settles inside the daughter bud and stabilizes close to the septin ring in the currently explored parameter regime [Fig. 5(e)]. An exciting feature of the spindle noticed via three-dimensional agent-based simulations is its proper orientation parallel to the mother-daughter axis, similar to the microscopic images in Fig. 1(a). While in the absence of MT buckling [Fig. 5(d)], the spindle inside the daughter appears to be randomly oriented relative to the axis. Due to these differences in spindle orientation, the absolute position of the spindles in the absence and presence of MT buckling [Figs. 5(d) and 5(e)] may not be compared explicitly. Nevertheless, based on Figs. 5(d) and 5(e) we can say that the daughter cortex's high dynein density pulls the spindle deep inside the daughter bud. Unlike the one-dimensional analytical model, we do not observe any spindle collapse in the three-dimensional agent-based model. The plausible reasons are (a) difference in the dimensionality between the two models, (b) stochastic fluctuations in the agent-based model compared to no fluctuation in the one-dimensional analytical model, (c) dynamic changes in spindle orientation in the absence of MT buckling as discussed above in three-dimensional simulation, etc., as opposed to parallel orientation in one-dimensional model.

As the mechanics of spindle positioning is largely MT mediated [16,23,25], we tested the dependence of spindle positioning on the average MT length. From the analytical and the agent-based model analysis, we found that when the average MT length is 'too short' ($\sim 1\,\mu$m), the spindle is retained in the mother [Figs. 5(c) and 5(f)]. In other words, the nucleus is unable to migrate to the daughter bud.

We further observe that in the presence of MT buckling, the variation in average MT length above a threshold does not affect the spindle localization inside the daughter bud [Figs. 5(c) and 5(f)]. As a plausible explanation, we argue that when the average cMT length is above a threshold, a few cMTs always reach the cortex. At the cortex, the interaction of MT and molecular motors transduce pN order forces, which is sufficient to stabilize the spindle at the proper location. Nevertheless, the force due to a MT's buckling is considerably large compared to other relevant forces (Table S2 in the Supplemental Material [19]). Therefore, the buckling transition of only a few cMTs from the cortex produces sufficient forces dominating the spindle localization. The position of the spindle remains unaffected because (a) the buckling mediated forces pointing away from the mother and daughter bud cell cortex are oppositely directed [Fig. 2(c)], and 2(b) number of MTs undergoing buckling at mother and daughter bud cell cortex are similar on average. Therefore, in the buckling-dominated landscape, the forces directed away from the mother and daughter cell cortex nullify each other near the septin ring.

In the agent-based computational model described above, the stochastic effects come into the picture through the MT dynamic instability and MT-cell cortex interaction. While this is a crucial source of stochasticity, other sources, including attachment-detachment of molecular motors (occurring at much shorter timescales), could significantly influence the earlier model outcomes. Because of that, we introduced the feature of stochastic MT-dynein attachment-detachment in the existing model. A similar stochastic character is presented in the context of Bim1 as well. The description of the model framework with stochastic attachment-detachment and detailed results are reported in the Supplemental Material [19] (Fig. S8– S10 in the Supplemental Material [19]).

3. Spindle positioning: Comparison of the modeling outcomes with the experimental observations

In the experiment, we observe that upon dynein depletion, most of the cells have nuclei retained in the mother bud (Fig. S6(A) in the Supplemental Material [19]), which agrees with the model outcome [Fig. 5(d)]. Deletion of Bim1 also leads to faulty nuclear migration (Fig. 4(a) and Fig. S6(B) in the Supplemental Material [19]). While acquiring the statistics in Fig. S1 in the Supplemental Material [19], Figs. S6(A) and S6(B) in the Supplemental Material [19], we have considered only large budded cells having budding indices 0.65 and above. Since the budding index is an indicator of "time" [Fig. 1(e)], higher budding indices refer to the cells in which a considerable amount of time has elapsed after bud initiation. In most wild-type cells with budding indices above 0.65, the nuclei are settled in the daughter bud (Fig. S1 in the Supplemental Material [19]). Upon dynein depletion/Bim1 deletion, we observe more cells with budding indices above 0.65 have nuclei retained in the mother bud (Figs. S6(A) and S6(B) in the Supplemental Material [19]) because, in those cells, the nuclear migration is possibly delayed/impaired. The same conclusion can be gleaned from the statistics of the budding indices of unsegregated cells in Fig. S4(A) in the Supplemental Material [19]. Next, to understand if dynein and Bim1 both are required for nuclear migration, we generated a strain where dynein is depleted in the absence of Bim1 (GAL7-DYN1 bim1△) in the histone GFP-H4 tagged background. We quantified the percentages of cells exhibiting abnormal nuclear segregation or no segregation of nuclear masses in bim1△, GAL7-DYN1 and/or GAL7-DYN1 bim1△ strains and compared them with the control wild-type H99 strain (Fig. S4(B) in the Supplemental Material [19]). We observed a significant increase in the number of unbudded and large budded bi-nucleated cells upon simultaneous depletion of dynein and Bim1 compared to the control (Fig. S4(C) in the Supplemental Material [19]). This result indicates that both Bim1 and dynein are required for nuclear migration where simultaneous depletion of both proteins results in delayed nuclear migration due to which the nucleus divides inside the mother bud itself in the majority of GAL7-DYN1 bim1△ cells. A note on the quantification of the experimental data on nuclear migration is included in the Supplemental Material [19].

The modeling results showing the dependence of spindle localization on average MT length [denoted in Figs. 5(c) and 5(f)] reasonably corroborate with our experimental observations (Figs. S6(C) and S6(D) in the Supplemental Material [19]). We observe spindle localization inside the daughter bud near the septin ring in wild-type cells (Fig. 1(a) and Fig. S6(C) and Movie M1 in the Supplemental Material [19]). But in cells treated with nocodazole, the MT integrity is severely compromised (Fig. S6(D) in the Supplemental Material [19]). In that scenario, we do not observe any spindle localization

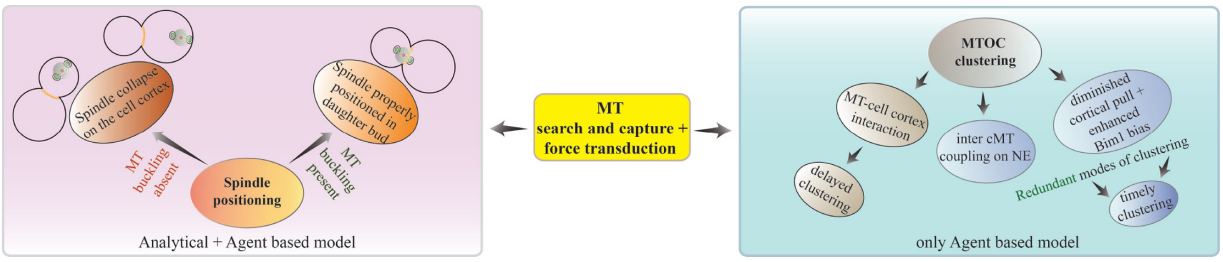

FIG. 6. Summary of model outcomes describing mechanistic aspects of MTOC clustering and spindle positioning in *C. neoformans*. The agent-based model depicts redundant mechanisms for the timely clustering of MTOCs. Inter cMT coupling at NE and/or cortical interaction of MTs with suppressed dynein pull and enhanced Bim1 bias may facilitate timely clustering, either independently or in unison. Furthermore, the analytical model supported by agent-based simulations suggests that proper spindle positioning in the daughter bud near the septin ring requires MT buckling from the cell cortex.

in the daughter bud (Fig. S6(D) in the Supplemental Material [19]).

To conclude, the spindle distance from the septin ring measured in the experiment (Fig. S5(E) in the Supplemental Material [19]) and estimated from the analytical [Fig. 5(c)] and computational models [Fig. 5(f)], reasonably agree with each other. Additional spindle characteristics predicted by the model are summarized in the Supplemental Material [19], Fig. S7 in the Supplemental Material [19], and Table S4 in the Supplemental Material [19]. Furthermore, we have also performed additional agent-based simulations to explore how varying dynein density profiles in mother and daughter cell cortex impact the timescales of MTOC clustering and nuclear migration (Fig. S13 in the Supplemental Material [19]). The results are discussed in the Supplemental Material in detail [19].

IV. DISCUSSION

Our theoretical approach combines (a) an agent-based computational model of MT "search and capture," and (b) an analytical model to explore the mitotic events in *C. neoformans*. With the help of the computational model, we examined the role of MT "search and capture" during MTOC clustering, nuclear migration, and spindle localization. Using the analytical model, we screened various combinations of the MT-based mechanistic forces and found plausible mechanical force balance conditions that may orchestrate proper spindle positioning.

Based on our modeling analysis, we draw the following conclusions (Fig. 6). The emergent timescales for MTOC clustering are similar in two scenarios; the design principles of which are based on (a) effective inter-MTOC attraction due to minus end-directed motor crosslinking between grazing antiparallel MTs on the NE and (b) effective drift of all the MTOCs toward the septin ring due to Bim1 mediated cortical bias with diminished dynein pull from the cortex. The clustering timescales go down with the minus-end motor mediated inward force at the MT-MT overlap in the first scenario. In the latter one, the clustering timescales go up with the net cortical dynein pull on the MTs. From a model perspective, the comparable timescales of these two independent clustering mechanisms indicate a possible redundancy between the two mechanisms [Figs. 3(d) and 3(e)]. Furthermore, our analytical model qualitatively highlights the mechanical requirements for proper spindle positioning by screening various MT-based forces. It has been suggested that the plane of mitotic division is defined by this stable positioning of the spindle inside the daughter bud with spindle orientation almost parallel to the axis joining the centers of the mother and daughter buds [14,16,52]. Our model shows that in the presence of two opposing forces, instantaneous cortical push and dynein pull (no MT buckling), the spindle collapses onto the cortex. Additional force due to MT buckling at the mother and daughter cortex is essential to restore the spindle's stable positioning near the septin ring. A key reason is the force due to buckling that scales with the inverse square of the MT length. Thus, when the spindle is close to the cortex, buckling MTs strongly push it away, preventing the collapse. The analytical model also shows several interesting positions of the spindle, which are unstable. The one-dimensional model can be extended to higher dimensions, including several important characteristic degrees of freedom (e.g., the orientation of the spindle, the angular displacement of the SPBs, etc.) in the analysis.

In the agent-based model, a major source of fluctuations is the stochastic MT dynamics manifesting the random switch between the states of polymerization and depolymerization [1,43,44,47]. In the mathematical model, the stochastic MT dynamics are not explicitly considered; the MT length distribution is exponential. In the agent-based model, stochasticity also comes into the picture through MT interaction with the cortex and cell membrane. When an MT elongates to the cortical region, the consequence is a probabilistic choice of the MT (a) undergoing catastrophe, (b) sliding along the cortex, and (c) buckling with the tip hinged or pivoted at the cell membrane. However, stochasticity stemming from the explicit binding or unbinding of the motors on MTs, collective "walking" of various groups of motors on the filaments, and associated modulations in force transmission via the MTs are not explicitly incorporated in the coarse-grained model. The stochastic effects arising from the thermal fluctuation at the molecular level and interactions of the "objects" with embedding viscous medium (e.g., the cytoplasm, the nucleoplasm) are not accounted for in the model.

We reiterate that the analytical model for spindle positioning is one-dimensional with simplified force expressions. We compared the analytical model results with the agent-based computational model to examine the physical basis and the

consistency of the spindle positioning attributes. One of the primary differences between the analytical and computational models is the stochastic effects. The agent-based model entails stochastic fluctuations stemming from the MT dynamic instability, a finite number of MTs, motor activity, etc. In contrast, the analytical model does not contain stochastic fluctuations and temporal degrees of freedom. Possibly, due to intrinsic fluctuations in the computational model, we do not observe any unstable spindle position.

The clustering of MT nucleating organelles in cells in general is of utmost biological importance. The clustering phenomenon is directly correlated with the process of cell division. In what follows, we briefly compare two such distinct clustering processes (including the one presented in this study), which involve centrosomes and MTOCs. During mitosis, cells self-organize the spindle to facilitate nuclear division, and for a faithful division, it is essential to have a bipolar spindle. The reason is that the sister chromatids require to partition into two opposite poles and settle in two daughter progeny. In mammalian cells, the prevalence of more than two centrosomes at the beginning of mitosis can generally be linked to multipolar spindle formation [23]. Multipolar spindles and the presence of more than two centrosomes or MTOCs often lead to chromosome instability, aneuploidy, erroneous attachments of chromosomes, and various other defects of chromosome segregation hindering faithful division. Recent studies highlight an interesting pathway of bypassing these defects where multiple centrosomes or MTOCs assemble into two groups or poles, making way for bipolar spindle formation in multi-centrosome or multi-MTOC cells. The process of converging multiple centrosomes into two poles during spindle formation is often termed "centrosome clustering" [23,53–55]. However, in the context of MTOC clustering in *C. neoformans*, the pathway for grouping the MTOCs into two poles turns out to be different. In *C. neoformans* we observe that MTOCs dynamically move toward each other along the outer NE's surface and eventually fuse, forming the SPB. During this process, KTs are found to colocalize with the MTOCs [Figs. 1(b)–1(d)] [20]. Unlike centrosome clustering resulting in two independent poles, MTOCs cluster into a single pole. The clustered pole, namely the SPB, subsequently duplicates into two SPBs paving the way for bipolar spindle formation.

In the context of "real" spindle, it has been suggested that MT bundling proteins (such as Ase1/PRC1) influences the spindle assembly process [56] and chromosome alignment [57,58]. The role of these proteins in directed force generation at the MT-MT overlaps was also studied previously [59,60]. An experimental investigation in *C. neoformans* in this direction, supported by theoretical modeling, would be a worthy future endeavor.

Our modeling results indicate that Bim1 mediated cortical bias plays a crucial role in MTOC clustering and nuclear migration. But, the molecular mechanisms via which Bim1 in concert with other regulatory factors influences the nuclear migration process is still unclear. To that end, at present, our knowledge regarding the molecular details of the spindle movement toward the septin ring is also limited. This is currently being investigated as an independent study. In addition to this, it would be interesting to experimentally probe the predicted Bim1 biased (suppressed dynein) regime (for MTOC clustering time) by adding dynein inhibitors at different concentrations in a time-lapse experiment.

Previously, the mechanics of MT aster positioning has been studied with considerable details in various contexts [61–63]. It has been suggested that both pushing and pulling forces (primarily relative to the cell boundary) govern the force balance landscape necessary for MT aster positioning. The mechanical conditions for a stable centering position for an MT aster within a confined geometry are: (a) pushing forces in tandem with MT catastrophe in the cytoplasm before the MTs hit the cell boundary; (b) pulling forces in tandem with MT sliding/slippage at cell cortex [63]. In the context of *C. neoformans*, we observe that the stable spindle positioning near the septin ring is strongly supported by the pushing forces (including buckling), which conforms with the condition (a). However, we do not observe stable spindle positioning near the septin ring in the currently explored parameter regime when the cortical pull is acting alone (Fig. S7(B) in the Supplemental Material [19]) or in combination with the instantaneous push (Fig. 5(a) and Figs. S7(B) and S7(D), S7(E) in the Supplemental Material [19]). In special cases when (a) the average MT length is significantly large compared to the cell size, (b) there are many cMTs or (c) cMT segments that keep sliding inside the cortex, the cortical pull may facilitate stable spindle positioning near the septin ring. Nevertheless, experiments indicate that the cMT number per SPB is limited and the average MT length is of the order of the cell size in *C. neoformans* [14,16] restricting the currently explored *in silico* parameter regime. Therefore, exploring the possibility of pulling mediated "stable centering" in the current context is possibly beyond the scope of the models presented here. Taking cues from other mechanistic models of MT aster positioning [61–64], a detailed mathematical model can be designed to elucidate the mechanics of spindle positioning further.

Moreover, within the parameter range studied, our model outcomes connote that MT buckling is essential (together with cortical pull and instantaneous push) for spindle centering near the septin ring. MTs are found to be in a buckled configuration in many cell types, including the budding yeast and fission yeast [65,66]. Several studies in literature explored the MT buckling phenomenon in the context of individual MTs as well as MT bundles at different experimental conditions as well as via utilizing theoretical approaches [45,46,67–72]. It will be a worthy future goal to experimentally test the role of MT buckling in spindle positioning in *C. neoformans*.

In summary, we constructed a phenomenology-based model that consistently explores spindle assembly aspects during mitotic cell division in the current study. Using the model, we have elucidated several important features of MTOC clustering, nuclear migration, and spindle positioning, largely from a mechanistic point of view (Fig. 6). While attempting to understand these processes in the light of dominant microtubule-based forces (e.g., buckling or pulling from the cortex), we ignored weaker forces that may arise from sources *viz*, actin turnover, other molecular motors, thermal fluctuations, etc. Nevertheless, all these forces are important, and a more realistic model should incorporate them in our future projects. Note that the attributes of the dynamic

processes involved in the mitotic cell cycle differ widely across different cell types. Different organisms evolved (with increasing complexity at the molecular level) to self-engineer the process of cell division. Thus, investigating the mechanistic principles of cell division across different organisms using a systems biology-based approach in collaboration with molecular biology experiments stands as the subject of future research. In other words, since there is no "the" spindle [73], a worthy long-term goal would be to develop an integrated "toolbox" using our existing in silico setup (codes and formalisms) to study MT-spindle mechanics across organisms in a context dependent manner. To carry out this task, we reiterate that a synergistic marriage between experiment and theoretical modeling is an essential guiding approach.

ACKNOWLEDGMENTS

This work was supported by the fellowship from SERB (Science and Engineering Research Board), Department of Science and Technology (DST), India (Grant No. EMR/2017/001346) to R.P. and Tata Innovation Fellowship (Grant No. BT/HRD/35/01/03/2017) to K.S. K.S. acknowledges the J.C. Bose National Fellowship from Science and Engineering Research Board (SERB) (Grant No. JCB/2020/000021), Government of India and a research grant from SERB (Grant No. CRG/2019/005549). S.C. was supported by a fellowship from the University Grants Commission (UGC), India. S.S. was supported by the fellowship from INSPIRE (No. IF131156) program DST, India. N.V. was supported by fellowships (No. 09/733 (0253)/219-EMR-I and No. 9/733 (0161)/2011-EMR-I) from Council of Scientific & Industrial Research (CSIR), India. P.S. is a senior research fellow supported by JNCASR, India.

R.P. and K.S. conceived and directed the study; S.C. and R.P. wrote the manuscript with K.S.; S.C. and S.S. performed the theoretical modeling, N.V. and P.S. performed experiments and analyzed data along with other coauthors. All coauthors contributed to the editing of the revised manuscript and approved the content.

[1] M. Dogterom and S. Leibler, Phys. Rev. Lett. **70**, 1347 (1993).
[2] J. Wu and A. Akhmanova, Annu. Rev. Cell Dev. Biol. **33**, 51 (2017).
[3] M. Bornens, Science **335**, 422 (2012).
[4] P. T. Conduit, A. Wainman, and J. W. Raff, Nat. Rev. Mol. Cell Biol. **16**, 611 (2015).
[5] V. Rodionov, E. Nadezhdina, and G. Borisy, Proc. Natl. Acad. Sci. USA **96**, 115 (1999).
[6] K. Chabin-Brion, J. Marceiller, F. Perez, C. Settegrana, A. Drechou, G. Durand, and C. Poüs, Mol. Biol. Cell **12**, 2047 (2001).
[7] L. Hurtado, C. Caballero, M. P. Gavilan, J. Cardenas, M. Bornens, and R. M. Rios, J. Cell Biol. **193**, 917 (2011).
[8] T. Vinogradova, R. Paul, A. D. Grimaldi, J. Loncarek, P. M. Miller, D. Yampolsky, V. Magidson, A. Khodjakov, A. Mogilner, and I. Kaverina, Mol. Biol. Cell **23**, 820 (2012).
[9] T. Vinogradova, P. M. Miller, and I. Kaverina, Cell Cycle **8**, 2168 (2009).
[10] J. Paz and J. Lüders, Trends Cell Biol. **28**, 176 (2018).
[11] J. V. Kilmartin, Philos. Trans. R. Soc. Lond. B Biol. Sci. **369**, 20130456 (2014).
[12] T. chen Lin, A. Neuner, and E. Schiebel, Trends Cell Biol. **25**, 296 (2015).
[13] T. chen Lin, A. Neuner, Y. T. Schlosser, A. N. Scharf, L. Weber, and E. Schiebel, Elife **3**, e02208 (2014).
[14] S. Sutradhar, V. Yadav, S. Sridhar, L. Sreekumar, D. Bhattacharyya, S. K. Ghosh, R. Paul, and K. Sanyal, Mol. Biol. Cell **26**, 3954 (2015).
[15] L. Kozubowski, V. Yadav, G. Chatterjee, S. Sridhar, M. Yamaguchi, S. Kawamoto, I. Bose, J. Heitman, and K. Sanyal, mBio **4**, 00614 (2013).
[16] N. Varshney, S. Som, S. Chatterjee, S. Sridhar, D. Bhattacharyya, R. Paul, and K. Sanyal, PLoS Genet **15**, e1007959 (2019).
[17] J. Heitman, Fungal Biol. Rev. **25**, 48 (2011).
[18] G. Janbon, K. Ormerod, D. Paulet, E. B. 3rd, V. Yadav, G. Chatterjee, N. Mullapudi, C. Hon, R. Billmyre, F. Brunel, Y. Bahn, W. Chen, Y. Chen, E. Chow, J. Coppee, A. Floyd-Averette, C. Gaillardin, K. Gerik, J. Goldberg, S. Gonzalez-Hilarion *et al.*, PLoS Genet. **10**, e1004261 (2014).
[19] See Supplemental Material at http://link.aps.org/supplemental/10.1103/PhysRevE.104.034402 for the BlparaBrpar experimental protocol, BlparbBrpar quantification of the experimental data on nuclear migration, BlparcBrpar simulation procedure, BlpardBrpar mathematical model for spindle positioning, BlpareBrpar additional numerical analysis of MTOC clustering Blparagent-based modelBrpar, and spindle positioning Blparanalytical modelBrpar, BlparfBrpar effects of stochastic attachment-detachment of dynein, Bim1 on MTOC clustering and nuclear migration, BlpargBrpar supplemental figures S1–S13, BlparhBrpar captions for supplemental movies M1–M4, BlpariBrpar supplemental tables S1–S4, and BlparjBrpar supplemental references [74–97].
[20] V. Yadav and K. Sanyal, mSphere **3**, e00190 (2018).
[21] M. Yamaguchi, S. K. Biswas, Y. Kuwabara, M. Ohkusu, M. Shimizu, and K. Takeo, J. Electron Microsc. **59**, 165 (2010).
[22] A. Gladfelter and J. Berman, Nat. Rev. Microbiol. **7**, 875 (2009).
[23] S. Chatterjee, A. Sarkar, J. Zhu, A. Khodjakov, A. Mogilner, and R. Paul, Biophys. J. **119**, 434 (2020).
[24] C. G. Rasmussen, J. A. Humphries, and L. G. Smith, Annu. Rev. Plant Biol. **62**, 387 (2011).
[25] F. J. McNally, J. Cell Biol. **200**, 131 (2013).
[26] M. Théry, A. Jiménez-Dalmaroni, V. Racine, M. Bornens, and F. Julicher, Nature (London) **447**, 493 (2007).
[27] N. Minc, D. Burgess, and F. Chang, Cell **144**, 414 (2011).
[28] G. Gay, T. Courtheoux, C. Reyes, S. Tournier, and Y. Gachet, J. Cell Biol. **196**, 757 (2012).
[29] N. Pavin and I. M. Tolic, Annu. Rev. Biophys. **45**, 279 (2016).

[30] A. V. Zaytsev, D. Segura-Pena, M. Godzi, A. Calderon, E. R. Ballister, R. Stamatov, A. M. Mayo, L. Peterson, B. E. Black, F. I. Ataullakhanov, M. A. Lampson, and E. L. Grishchuk, Elife **5**, e10644 (2016).

[31] M. W. Elting, M. Prakash, D. B. Udy, and S. Dumont, Curr. Biol. **27**, 2112 (2017).

[32] J. Li, L. Cheng, and H. Jiang, Mol. Biol. Cell **30**, 2458 (2019).

[33] G. Letort, I. Bennabia, S. Dmitrieffb, F. Nedelec, M.-H. Verlhaca, and M.-E. Terreta, Mol. Biol. Cell **30**, 863 (2019).

[34] A. R. Lamson, C. J. Edelmaier, M. A. Glaser, and M. D. Betterton, Biophys. J. **116**, 1719 (2019).

[35] N. P. Ferenz, R. Paul, C. Fagerstrom, A. Mogilner, and P. Wadsworth, Curr. Biol. **19**, 1833 (2009).

[36] F. Nedelec, J. Cell. Biol. **158**, 1005 (2002).

[37] R. Wollman, G. Civelekoglu-Scholey, J. M. Scholey, and A. Mogilner, Mol. Syst. Biol. **4**, 195 (2008).

[38] B. Rubinstein, K. Larripa, P. Sommi, and A. Mogilner, Phys. Biol. **6**, 016005 (2009).

[39] I. Kalinina, A. Nandi, P. Delivani, M. R. Chacón, A. H. Klemm, D. Ramunno-Johnson, A. Krull, B. Lindner, N. Pavin, and I. M. Tolić-Nørrelykke, Nat. Cell. Biol. **15**, 82 (2013).

[40] H. Maiato, A. M. Gomes, F. Sousa, and M. Barisic, Biology **6**, 13 (2017).

[41] S. Som, S. Chatterjee, and R. Paul, Phys. Rev. E **99**, 012409 (2019).

[42] M. W. Staudt, E. K. Kruzel, K. Shimizu, and C. M. Hull, Fungal Genet. Biol. **47**, 310 (2010).

[43] T. Mitchison and M. Kirschner, Nature (London) **312**, 237 (1984).

[44] T. E. Holy and S. Leibler, Proc. Natl. Acad. Sci. USA **91**, 5682 (1994).

[45] F. Gittes, E. Meyhöfer, S. Baek, and J. Howard, Biophys. J. **70**, 418 (1996).

[46] M. Soheilypour, M. Peyro, S. J. Peter, and M. R. Mofrad, Biophys. J. **108**, 1718 (2015).

[47] M. Kirschner and T. Mitchison, Cell **45**, 329 (1986).

[48] L. Winters, I. Ban, M. Prelogović, I. Kalinina, N. Pavin, and I. M. Tolić, BMC Biol. **17**, 42 (2019).

[49] S. Baumgärtner and I. M. Tolić, PLoS ONE **9**, e93781 (2014).

[50] G.Civelekoglu-Scholey, D.J.Sharp, A. Mogilner, and J. Scholey, Biophys. J. **19**, 3966 (2006).

[51] R. Farhadifar, C. F. Baer, A. C. Valfort, E. C. Andersen, T. Muller-Reichert, M. Delattre, and D. J. Needleman, Curr. Biol. **25**, 732 (2015).

[52] M. K. Balasubramanian, E. Bi, and M. Glotzer, Curr. Biol. **14**, R806 (2004).

[53] M. Kwon, S. A. Godinho, N. S. Chandhok, N. J. Ganem, A. Azioune, M. Thery, and D. Pellman, Genes & Dev. **22**, 2189 (2008).

[54] F. Gergely and R. Basto, Genes & Dev. **22**, 2291 (2008).

[55] V. Marthiens, M. Piel, and R. Basto, J. Cell Sci. **125**, 3281 (2012).

[56] S. A. Rincon, A. Lamson, R. Blackwell, V. Syrovatkina, V. Fraisier, A. Paoletti, M. D. Betterton, and P. T. Tran, Nat. Commun. **8**, 15286 (2017).

[57] M. Jagrić, P. Risteski, J. Martinčić, A. Milas, and I. M. Tolić, eLife **10**, e61170 (2021).

[58] B. Polak, P. Risteski, S. Lesjak, and I. M. Tolić, EMBO Rep. **18**, 217 (2017).

[59] Z. Lansky, M. Braun, A. Lüdecke, P. R. ten Wolde, M. E. Janson, and S. Diez, Cell **160**, 1159 (2015).

[60] I. Gaska, M. E. Armstrong, A. Alfieri, and S. Forth, Dev. Cell **54**, 367 (2020).

[61] L. Laan, N. Pavin, J. H. J, G. Romet-Lemonne, M. van Duijn, M. P. Lopez, R. D. Vale, F. Jülicher, S. L. Reck-Peterson, and M. Dogterom, Cell **148**, 502 (2012).

[62] N. Pavin, L. Laan, R. Ma, M. Dogterom, and F. Jülicher, New J. Phys. **14**, 105025 (2012).

[63] R. Ma, L. Laan, M. Dogterom, N. Pavin, and F. Jülicher, New J. Phys. **16**, 013018 (2014).

[64] S. W. Grill, K. Kruse, and F. Jülicher, Phys. Rev. Lett. **94**, 108104 (2005).

[65] S. L. Shaw, E. Yeh, P. Maddox, E. D. Salmon, and K. Bloom, J. Cell Biol. **139**, 985 (1997).

[66] D. Foethke, T. Makushok, D. Brunner, and F. Nédéléc, Mol. Syst. Biol. **5**, 241 (2009).

[67] M. Kurachi, M. Hoshi, and H. Tashiro, Cell Motil. Cytoskel. **30**, 221 (1995).

[68] M. Elbaum, D. K. Fygenson, and A. Libchaber, Phys. Rev. Lett. **76**, 4078 (1996).

[69] D. K. Fygenson, J. F. Marko, and A. Libchaber, Phys. Rev. Lett. **79**, 4497 (1996).

[70] T. Li, J. Biomech. **41**, 1722 (2008).

[71] J. Howard, Phys. Biol. **3**, 54 (2006).

[72] C. P. Brangwynne, F. C. MacKintosh, and D. A. Weitz, J. Cell Biol. **173**, 733 (2006).

[73] A. Mogilner and E. Craig, J. Cell Sci. **123**, 3435 (2010).

[74] R. Davidson, M. Cruz, R. Sia, B. Allen, J. Alspaugh, and J. Heitman, Fungal Genet. Biol. **29(1)**, 38 (2000).

[75] Z. Bertalan, Z. Budrikis, C. A. M. L. Porta, and S. Zapperi, PLoS ONE **10**, e0141305 (2015).

[76] R. Wollman, E. Cytrynbaum, J. Jones, T. Meyer, J. Scholey, and A. Mogilner, Curr. Biol. **15**, 828 (2005).

[77] A. Sarkar, H. Rieger, and R. Paul, Biophys. J. **116**, 2079 (2019).

[78] M. J. I. Muller, S. Klumpp, and R. Lipowsky, Proc. Natl. Acad. Sci. USA **105**, 4609 (2008).

[79] D. Ghanti, R. W. Friddle, and D. Chowdhury, Phys. Rev. E **98**, 042415 (2018).

[80] H.A.Kramers, Physica **7**, 284 (1940).

[81] G. Bell, Science **200**, 618 (1978).

[82] A. Kramer, B. Maier, and J. Bartek, Mol. Oncol. **5**, 324 (2011).

[83] M. P. Singh, R. Mallik, S. P. Gross, and C. C. Yu, Proc. Natl. Acad. Sci. USA **102**, 12059 (2005).

[84] S. J. King and T. A. Schroer, Nature Cell Biol. **2**, 20 (2000).

[85] S. L. Reck-Peterson, A. Yildiz, A. P.Carter, A. Gennerich, N. Zhang, and R. D.Vale, Cell **126**, 335 (2006).

[86] R. Mallik, B. C. Carter, S. A. Lex, S. J. King, and S. P. Gross, Nature (London) **427**, 649 (2004).

[87] I.-J. Lee, N. Wang, W. Hu, K. Schott, J. Bahler, T. H. G. Jr., J. R. Pringle, L.-L. Du, and J.-Q. Wu, Mol. Biol. Cell **25**, 2735 (2014).

[88] C. Seybold and E. Schiebel, Curr. Biol. **23**, R858 (2013).

[89] G. Fink, I. Schuchardt, J. Colombelli, E. Stelzer, and G. Steinberg, EMBO J. **25**, 4897 (2006).

[90] K. R. Finley, K. J. Bouchonville, A. Quick, and J. Berman, J. Cell Sci. **121**, 466 (2008).

[91] G. Letort, F. Nedelec, L. Blanchoin, and M. Thery, Mol. Biol. Cell **27**, 2833 (2016).

[92] M. Dogterom and B. Yurke, Science **278**, 856 (1997).
[93] V. Soppina, A. K. Rai, A. J. Ramaiya, P. Barak, and R. Mallik, Proc. Natl. Acad. Sci. USA **106**, 19381 (2009).
[94] S. M. Markus, K. M. Plevock, B. J. S. Germain, J. J. Punch, C. W. Meaden, and W. Lee, Cytoskeleton **68**, 157 (2011).
[95] A. P. Joglekar and A. J. Hunt, Biophys. J. **83**, 42 (2002).
[96] S. Sau, S. Sutradhar, R. Paul, and P. Sinha, PLoS One **9**, e101294 (2014).
[97] A. Rodal, L. K. L, B. Goode, D. D. DG, and J. Hartwig, Mol. Biol. Cell. **16**, 372 (2005).